

# Mechanical properties of friction induced nanocrystalline pearlitic steel

**Bentejui Medina-Clavijo** (✉ [bemc@sci.one](mailto:bemc@sci.one))

CIC nanoGUNE BRTA

**Jorge Rafael-Velayarce**

Saarland University

**Evgenii Modin**

CIC nanoGUNE BRTA

**Mikel Saez-de-Buruaga**

Mondragon Unibertsitatea

**Daniel Soler**

Mondragon Unibertsitatea

**Christian Motz**

Saarland University

**Pedro Jose Arrazola**

Mondragon Unibertsitatea

**Andrey Chuvilin**

CIC nanoGUNE BRTA

---

## Research Article

**Keywords:** Mechanical properties, Microstructure, Dynamic recrystallization, Metal cutting, Machining

**Posted Date:** February 24th, 2022

**DOI:** <https://doi.org/10.21203/rs.3.rs-1332231/v1>

**License:**  This work is licensed under a Creative Commons Attribution 4.0 International License.

[Read Full License](#)

---

# Abstract

Nanocrystalline variants of commercially available alloys have shown the potential of boosting the mechanical properties retaining a feasible supply chain. One approach to achieve these nanostructures reside in frictional treatments on parts, leading to differential refinement in surface and bulk. In this work the machining method is considered as a testing platform to study frictional nanostructured steel, which assembly is stabilized by fast cooling at the chip. The analysis of the mechanical properties has shown extraordinary results at the surface, over 2000 MPa of strength on AISI1045 steel, more than three times the strength of the base material, demonstrating at the same time a reduction of 15% in the elastic modulus. The microscopic analysis suggests a reassembly of the elements in a new lattice of carbon supersaturated nano-ferrite.

## Introduction

Nanostructured metallic materials typically have very different mechanical properties comparing to their coarse-grained counterparts. As a consequence of the reduction of mobility of linear defects (dislocations), confined between close grain boundaries (GBs), the hardness and ultimate strength of nanostructured metals is very high, which might provide certain technological benefits. Traditional methods to fabricate nanostructured metals have been classified as bottom-up and top-down<sup>1</sup>. Bottom-up refers to the assembly of the material by agglomeration of atoms or molecules (as a rule in non-equilibrium conditions), like processes based in vapor deposition or fast solidification, while the top-down approach consists of refining existing coarse structure mostly by severe plastic deformation<sup>2</sup> (SPD). SPD has been implemented in several techniques for material's bulk refinement, e.g., high pressure torsion<sup>3</sup> (HPT) or equal channel angular extrusion<sup>4</sup> (ECAE).

SPD techniques modify the whole workpiece, thus providing a new bulk material with unique properties defined by nanocrystallinity. The other class of techniques, yet substantially less studied and developed, involve only surface modification, which in many practical applications may be even beneficial for the piece consumer properties. This can be achieved by modification of a surface by the friction with a tool in a process similar to friction welding or high-speed cutting.

The formation of surface layers with sub-micrometer grains has been reported in machining or tribological experiments<sup>5,6</sup>, however one could expect that the formation of these structures corresponds to different conditions comparing to the nano-structuring processes in bulk material. For instance, the characteristic strain rate in the friction area during machining cover values of  $10^3 - 10^8 \text{ s}^{-1}$ <sup>7</sup>, where the strain-induced heating has a major impact. Temperatures over 0.5 and up to 0.8 of the melting temperature are common in machining, activating processes, like dynamics recrystallization<sup>8</sup>. Investigations on the chip side frictioning against the tool suggests not only a strong refinement<sup>6,9,10</sup> but also substantial transformations in the distribution of the elements of the alloy. The grain size observed under friction surface of 1045 AISI steel remained below 100 nm in the top layer. Crystal size refinement

was accompanied by a strong redistribution of the alloying elements from the original pearlitic structure, and by a reduction of the residual stress as a consequence of a process of dynamic recrystallization<sup>11</sup>. While efficient procedures to study the intermediate events during fast friction induced transformations of the surface of metals are emerging<sup>12-14</sup>, current setups to study machining represent a platform to learn about conditions and structures of these nano-structured materials, which are efficiently preserved by the ultra-fast cooling happening in chips after cutting<sup>8</sup>.

Properties of bulk nanostructures metals are well known and characterized by an increase of the strength and a detrimental thermal stability, common for both bottom-up and top-down fabrication methods<sup>15</sup>. At the same time the mechanical properties of final and intermediate stages of thin layers of friction-induced nanomaterials (FIN) are, to the knowledge of the authors, only recently matter of deep analysis, hampered by the typical size (of some microns) of the layer thickness affected by friction. Pillar testing experiments have shown that this material develop different collapsing tendencies under ultimate compression a high material strength, hence possess fundamentally different deformation mechanics<sup>16</sup>. A very promising finding of Zhou et al. suggests that, in terms of thermal stability, these structures demonstrate a strong deviation from the known nanomaterials<sup>17</sup>, i.e., FINs depict an overwelding thermal stability, comparable to over-micron structured alloys. These structures were obtained by surface sliding in cryogenic conditions, leading to a fast local self-heating due to large strain rate and consequent fast cooling. This opens further applications of nanomaterials for industrial applications, since the long-term stability could be solved with the proper mechanical refining in the surface. Similar grain sizes can be readily obtained in the chip after fast machining of the steel, where the material is heated up to 0.6 the melting temperature ( $T_m$ ) by enormous strain rate and cooled down in timeframe of milliseconds<sup>8</sup>. Thus, this process can provide a benchmark material to test the properties of potential future nano-structured alloys.

In this work we present a study of the FIN obtained from 1045 AISI steel in high-speed cutting process. Morphological, structural, chemical and mechanical test has been performed on the samples. A set of pillar compression along with the crystal size gradient in chip surface has permitted the evaluation of bulk-equivalent ultimate strength at different grain sizes, down to sub-100 nm crystalline material.

## Results

After machining, the material in the chip depicts a strong structure refinement. Figure 1 shows a channeling contrast focused ion beam (FIB)<sup>18</sup> image of the cross-section of the chip. The surface being in contact with the tool is at the top of the image, red dashed line separates two areas with distinctly different structure. Under the line, the microstructure reveals a shear direction with a parallel distribution of the long axis of the crystals. Closer to the surface, where the effects of friction should be more evident the crystallites are very small and do not show signs of a particular shear direction. This structure is typical for the material undergone dynamic recrystallization (DRX) in FIN samples and is known as a “white layer” in corresponding literature<sup>19</sup>. Both sheared and recrystallized structures have been

mechanically tested in the areas indicated by yellow boxes. The pillar compression tests covered both recrystallized and sheared material, while beam bending was only performed at the very surface sub-100 nm grained material due to necessity for side access.

In Fig. 1a a certain gradient of grain sizes can be observed, from sub-micron at the boundary of the DRX layer and down to 80 nanometers in the top surface (Fig. 1b), which comparing to the original material structure denotes a two orders of magnitude reduction in grain size. Moreover, in contrast to the original material, which has pearlite colonies in 75% of the volume, the recrystallized material presents a lack of cementite lamellae and a few visible carbide particles (see red circles in Fig. 1b and Fig. 2). FEM simulations with similar conditions suggested that the recrystallized area develop strains over 300% (see details in Methods), introducing energy to initiate a DRX process.

DRX area has been analyzed by scanning transmission electron microscopy (STEM). Figure 2 (left) shows A STEM image of a few grains from DRX layer, and corresponding EDX maps for iron (center) and carbon (right) obtained from the same region. With the exception of a small particle, the chemical analysis revealed that carbon is homogeneously distributed without segregation in the grain boundaries.

The crystallographic structure of the recrystallized and sheared area has been further analyzed by (transmission) electron back scatter diffraction ((t)-EBSD) in a scanning electron microscope (SEM). Figure 3a shows t-EBSD map of the material at the very surface of DRX layer (depth increases from top to the bottom of the map), Fig. 3b shows corresponding kernel average misorientation (KAM) map. EBSD data on Fig. 3 (c) and (d) provide a broader view of DRX layer on top and sheared region at the bottom. The sheared layer shows a structure with a prominent shear deformation, where grains/sub-grains with similar orientation are aligned in lamellae at oblique angle to the top surface. In contrast, the crystals in DRX layer have equiaxial shape without prominent signs of shear. Pole figures (Fig. 3e,f) show significantly more prominent crystal texture of the sheared layer as compared to DRX. KAM map is an illustrative indicator of the density of geometrically necessary dislocations<sup>20</sup>. Dislocation density is visually substantially lower in DRX layer (Fig. 3b,d) confirming structure reorganization (internal strain release) by re-crystallization.

For the mechanical tests, pillars of 6, 3 and 2  $\mu\text{m}$  of diameter have been milled by FIB on the cross-section at the very surface region and down to 63  $\mu\text{m}$  deep into the sheared layer. The pillars height for each case is 3 times the diameter. For each case, pillar strength has been calculated at a strain of 5%. Figure 4 shows the values of strength depending on the distance of the center of the pillar to the edge. The pillar diameter did not make a notable influence on the strength, indicating no size-effect on the measurements. In contrast, the strength strongly depends on the distance to the surface, i.e. on the grain size and on the strain state of the material. Figure 5 shows individual stress-strain plots of 2  $\mu\text{m}$  diameter pillars located at different distances from the surface.

The curve representing the sheared layer (29  $\mu\text{m}$  to the edge) demonstrates the maximum strength value around 1300 MPa, while at the top of the DRX layer (2.5  $\mu\text{m}$  to the edge) the maximum strength may

exceed 2000 MPa. FIB images of compressed pillars (Fig. 6) reveal the difference in deformation behavior of the pillars: while nanocrystalline pillar from DRX layer shows a regular structure of nano-grains that deform homogeneously, the pillar from the 29  $\mu\text{m}$  depth contains the deformed pearlitic layers which determine the easy sliding plane.

One of the features observed on the curves on Fig. 5 is a light reduction of the elastic modulus in the pillars in the recrystallized area. Variation of elastic modulus can indicate a fundamental change in atomic structure and/or interatomic distances<sup>21</sup>, thus pointing to some redistribution of the components in the lattice.

However, determining the elastic modulus in micro-compression experiments leads hardly reproducible results, small misalignments use to change notably the results. In order to obtain an accurate value of the elastic modulus beam bending experiments were performed in the proximity of the edge, inside the area affected by DRX. The method of beam bending was previously demonstrated to be suitable for elastic modulus measurement at small scales<sup>22</sup>. It provides good sensitivity to modulus calculation and, contrary to pillar compression, it is relatively agnostic to small geometric misalignments. Beams with a width of 5  $\mu\text{m}$  and 25  $\mu\text{m}$  long have been tested by flexion in-situ in SEM (Fig. 7). Calculations of elastic modulus have been made following the procedure described by Demir et al.<sup>23</sup>. The set of beam bending tests has led to reproducible values of elastic modulus rounding 178 GPa, with a standard deviation of 5 GPa.

## Discussion

In classical SDP methods for structure refinement, the achievable grain size, also known as grain size of saturation, is defined by the competition between the rate of structure fragmentation and grain coarsening<sup>24</sup>: while sustained large strains break down the microstructure into smaller and defective grains, high temperature activates grain boundary and lattice diffusion of atoms, the later drives diffusive repairing of crystallographic defects and coarsening of the grains<sup>25</sup>. These processes happen on relatively long timescales, which are unavoidable in bulk processing. The scenario of frictional surface structure refinement is slightly different. Though similar large strains are generated in a subsurface region upon friction e.g., during machining, this happens very locally and on the timescale of milliseconds. Consequently, the area is rapidly cooled in approximately the same timeframe. As an activation energy of boundary diffusion is substantially lower than the one of lattice diffusion the dominating process of structure relaxation in this case is rotational recrystallisation<sup>8</sup> driven by boundary diffusion. Grain coarsening does not have substantial impact in these short timeframes. This pushes the achievable grain size down to 100 nm and smaller. Fast cooling stabilizes the nano-structured layer, retaining this particular material assembly<sup>12</sup>. Grain size and residual internal strain distribution with the depth below the surface reflect the distribution of temperature field during the process and the time of exposition of the structure to high temperature. As both parameters have a strong dependence on the depth, the resulting structure also shows peculiar depth dependence of the grain sizes and residual strain.

The top layer, which is in a direct contact to the tool, accommodates the highest temperature, but is cooled very fast. There strain remains over 300% in the few microns closer to the tool contact. Consequently, highly strained material in this region relaxes (by rotational DRX) into (sub)100 nm strain-free grains, which have no time to grow. 5–10  $\mu\text{m}$  deeper into the bulk high temperature remains for a longer time and thus larger grains are observed. At 20  $\mu\text{m}$  depth the elevation of the temperature during processing and strains under 200% aren't sufficient to initiate diffusion and we observe highly strained material in this region. Figure 6 demonstrates, that pearlitic layers are preserved here, yet are strongly deformed.

On top of structure refining, this process in pearlitic steel also results in redistribution of carbon. In pristine material pearlite colonies occupy 3/4 of the volume, while in DRX layer we observe only singular carbon rich precipitates (Fig. 1b). This lack of carbides might indicate a scenario where carbon atoms diffuse to grain boundaries, but chemical analysis in Fig. 3 does not show an excess of carbon in grain boundaries. Carbon is mostly homogeneously distributed in the matrix of ferrite, reassembling the results of a number of authors reporting a super-saturated state of ferrite after cold working of pearlitic steel caused by severe plastic deformation<sup>26–28</sup>. Carbon dissolution in ferrite above saturation level has been unambiguously experimentally validated by atom probe tomography<sup>29</sup> on machined surfaces of martensitic steels. This supersaturated ferrite does not reproduce the structure of other metastable carbon-rich iron structures, like martensite or austenite. In contrary, it possesses relaxed ferrite structure with high carbon content and without carbon segregation.

Mechanical properties of the observed FIN layers were characterized by micromechanical testing methods: micropillar compression and micro-beam bending. Usage of micro-scale methods allows to obtain spatial distribution of properties in  $\sim 30 \mu\text{m}$  layer.

Experiments in pillar compression were designed to account for possible size effects, i.e. the dependence of the measurements on the pillar diameter due to dislocations starvation<sup>30 31</sup>, which typically cause an increase in measured strength in single crystals. The grains in FIN layer are well below 1  $\mu\text{m}$  and Fig. 4 clearly shows that there is no dependence of the measured strength on the pillar diameter, meaning we are measuring a real material strength, as expected from grains size is much smaller than the pillar, being the strength dominated by the smaller feature size, i.e. the grain size.

The strength of the nanostructured material in DRX layer is almost 3 times higher than that of the original AISI1045 steel -  $\sim 2000\text{MPa}$  against 500-700MPa in a pristine AISI1045. This is a typical trend in nanostructured metals, though for the first time measured in high carbon content steel. Figure 6 shows that the deformation and failure mechanisms in nanostructured material and in distorted pearlite may be substantially different. While pearlitic layers inclined to the strain direction provide “easy” sliding planes (Fig. 6), in the isotropic nanostructured material from the DRX layer there is no preferential “easy” direction, which in combination with the high density of the grain boundaries (serving as the sinks for dislocations) inhibits sliding and determines enhanced strength.

The other trend visible on Fig. 5 is the notable decrease of the slope of the elastic part of the strain/stress curves (elastic modulus) at increasing ultimate strength of the pillar. This qualitative observation on the pillar compression has been quantitatively evaluated in beam bending experiments (Fig. 7) - the measurements resulted in  $178 \pm 5$  GPa elastic modulus for the DRX layer, which is 12% less than the elastic modulus of pristine AISI1045. Decrease in elastic modulus by about 7% after rolling or tensile tests has been earlier reported<sup>132</sup>, linking metal defect generation with elastic modulus. Chen et al. have found a reduction of the elastic modulus in the order of 10% in the “white” (DRX) layer in friction processed Inconel 718<sup>33</sup>. This effect has been also observed in other metals with crystallite size below  $25 \text{ nm}^{34}$ , where the volume fraction of defects may infer certain characteristics of glasses, in particular the reduced elastic modulus<sup>35</sup>. Thus, the same process of structure refinement that makes the strength higher also brings down the elastic modulus.

In summary:

- FIN layer is generated from AISI1045 during machining, which is characterized by the gradient of crystal size and internal stress.
- The topmost  $5 \mu\text{m}$  of FIN layer undergoes rotational DRX and fast cooling, which preserves the crystal size at the level of 100 nm.
- Carbon distributes uniformly in ferrite lattice.
- Recrystallized layer has a strength of 2000 MPa, which is three times over the typical value of pristine AISI 1045 steel.
- Elastic modulus of nanostructured layer is reduced by 12% relative to pristine AISI1045.

## Methods

Chips generated during high speed orthogonal dry cutting of AISI 1045 annealed steel were used as representative samples of friction induced nanostructures. Dry machining was performed with uncoated P15 grade carbide cutting tools (WIDIA TPUN 160308 TTM), rake angle = 6 degrees and cutting-edge radius = 40  $\mu\text{m}$ . The feed rate was kept constant to 0.2 mm/rev, while the cutting speed 200 m·min<sup>-1</sup>. At these conditions the pristine material (a mean grain size of 7–9  $\mu\text{m}$ , and microstructure of pearlite and ferrite) undergo severe plastic deformation (over 200%) accompanied by high temperature (800 °C) and consequent fast cooling (approximately within 3 ms)<sup>36</sup>. High temperature initiates dynamic crystallization on the surface of severely deformed material and fast cooling freezes thus obtained nanocrystallites preventing grains coarsening<sup>8</sup>.

Chips were embedded in silver epoxy, polished and used for EBSD analysis. The same samples were utilized for fabrication and testing of micro-pillars. These pillars were made by FIB milling in two steps. First, a rough milling was performed with currents up to 9 nA. Subsequently, each pillar was exactly defined using ion current of 100 pA. Beams for bending tests were milled at the edges of the chips side polished without embedding; this was necessary to have access for milling from two sides. Beams of 2

and 5  $\mu\text{m}$  thickness have been milled by FIB with a first by a high current (9 nA), and afterwards a fine milling was performed at 1 nA. All the FIB nanofabrication was made on a DualBeam SEM/FIB instrument (Helios 600 DualBeam, FEI). STEM study was conducted on Titan 60–300 (FEI) equipped with an EDX RTEM (EDAX). (t-)EBSD data were obtained on Helios 600 DualBeam equipped with AMETEK EBSD camera and on Sigma SEM (Zeiss) equipped with Oxford Instruments EBSD camera.

Pillar compression tests were made using nano-indenter TriboIndenter TI 900 (Hysitron) equipped with a flat punch tip. Pillars have been compressed by displacement control at a strain rate of approximately  $40 \text{ s}^{-1}$ . Sneddon criteria was used for the correction of the base material deformation (Sneddon 1965). Experiments of beam bending were made in-situ in the chamber of the Sigma SEM microscope (Zeiss). The testing device in that case was nano-indenter UNAT-SEM2 (ASMEC). This in-situ nano-indenter was equipped with a tungsten tip milled by FIB to perform bending tests as in Fig. 8.

Software assisted modelling were used to calculate plastic strain of the material. The plastic strain values in the tool-chip contact area are higher than 300% considering results obtained with AdvantEdge (V7.9) commercial software (Fig. 9). Material and contact data employed in the simulation were taken from the software database. Cutting conditions and tool geometry and material were similar to those employed in experimental tests.

## Declarations

Acknowledgements (PLEASE MODIFY)

The authors acknowledge financial support from Basque government under the projects **Micromaquinte** (PI\_2014\_1\_116) and **Elkartek** 2018 (KK-2018/00001), and from the Spanish Ministry of Science, Innovation and Universities (the project MDM-2016-0618 of the Marie de Maeztu Units of Excellence Program and the coordinated **RETOS** projects RTI2018-095463-B-C21 and RTI2018-095463-B-C22 SURFNANOCUT) for their funding of the research presented in this paper.

## References

1. Zhang, X., Sun, C. & Fang, N. Manufacturing at Nanoscale: Top-Down, Bottom-up and System Engineering. *Journal of Nanoparticle Research* **6**, 125–130 (2004).
2. Bridgman, P. W. Effects of High Shearing Stress Combined with High Hydrostatic Pressure. *Phys. Rev.* **48**, 825–847 (1935).
3. Edalati, K. & Horita, Z. A review on high-pressure torsion (HPT) from 1935 to 1988. *Materials Science and Engineering: A* **652**, 325–352 (2016).
4. Rosochowski, A. & Olejnik, L. Numerical and physical modelling of plastic deformation in 2-turn equal channel angular extrusion. *Journal of Materials Processing Technology* **125–126**, 309–316 (2002).

5. Abdelali, H. B., Salem, W. B., Rech, J., Dogui, A. & Kapsa, P. Design and Modeling of Mechanical Systems. 541–548 (2013) doi:10.1007/978-3-642-37143-1.
6. Courbon, C. *et al.* Further insight into the chip formation of ferritic-pearlitic steels: Microstructural evolutions and associated thermo-mechanical loadings. *International Journal of Machine Tools and Manufacture* **77**, 34–46 (2014).
7. Childs, T. H. C., Maekawa, K., Obikawa, T. & Yamane, Y. *Metal Machining, Theory and applications*. (Elsevier, 2000).
8. Medina-Clavijo, B. *et al.* Microstructural aspects of the transition between two regimes in orthogonal cutting of AISI 1045 steel. *Journal of Materials Processing Technology* **260**, 87–96 (2018).
9. Mondelin, A., Valiorgue, F., Rech, J., Coret, M. & Feulvarch, E. Modeling of surface dynamic recrystallisation during the finish turning of the 15-5PH steel. *Procedia CIRP* **8**, 311–315 (2013).
10. Pu, C. L., Zhu, G., Yang, S. B., Yue, E. B. & Subramanian, S. V. Effect of dynamic recrystallization at tool-chip interface on accelerating tool wear during high-speed cutting of AISI1045 steel. *International Journal of Machine Tools and Manufacture* **100**, 72–80 (2016).
11. Courbon, C. *et al.* Towards a Physical FE Modelling of a Dry Cutting Operation: Influence of Dynamic Recrystallization When Machining AISI 1045. *Procedia CIRP* **8**, 516–521 (2013).
12. Medina-Clavijo, B. *et al.* In-SEM micro-machining reveals the origins of the size effect in the cutting energy. *Sci Rep* **11**, 2088 (2021).
13. Ameli Kalkhoran, S. N., Vahdati, M. & Yan, J. Effect of relative tool sharpness on subsurface damage and material recovery in nanometric cutting of mono-crystalline silicon: A molecular dynamics approach. *Materials Science in Semiconductor Processing* **108**, 104868 (2020).
14. Kurmanaeva, L. *et al.* Grain refinement and mechanical properties in ultrafine grained Pd and Pd–Ag alloys produced by HPT. *Materials Science and Engineering: A* **527**, 1776–1783 (2010).
15. Ames, M. *et al.* Unraveling the nature of room temperature grain growth in nanocrystalline materials. *Acta Materialia* **56**, 4255–4266 (2008).
16. Liao, Z. *et al.* On the influence of gamma prime upon machining of advanced nickel based superalloy. *CIRP Annals* **0**, 1–4 (2018).
17. Zhou, X., Li, X. Y. & Lu, K. Enhanced thermal stability of nanograined metals below a critical grain size - Supplementary. *Science* **360**, 526–530 (2018).
18. Yao, N. *Focused ion beam systems: Basics and Applications*. (Cambridge university press, 2007).
19. Liao, Z. *et al.* Surface integrity in metal machining - Part I: Fundamentals of surface characteristics and formation mechanisms. *International Journal of Machine Tools and Manufacture* **162**, 103687 (2021).
20. Calcagnotto, M., Ponge, D., Demir, E. & Raabe, D. Orientation gradients and geometrically necessary dislocations in ultrafine grained dual-phase steels studied by 2D and 3D EBSD. *Materials Science and Engineering: A* **527**, 2738–2746 (2010).
21. Padmavathi, D. A. Potential Energy Curves & Material Properties. *MSA* **02**, 97–104 (2011).

22. Rafael Velayarce, J., Zamanzade, M., Torrents Abad, O. & Motz, C. Influence of single and multiple slip conditions and temperature on the size effect in micro bending. *Acta Materialia* **154**, 325–333 (2018).
23. Demir, E. & Raabe, D. Mechanical and microstructural single-crystal Bauschinger effects: Observation of reversible plasticity in copper during bending. *Acta Materialia* **58**, 6055–6063 (2010).
24. Stüwe, H. P., Padilha, A. F. & Siciliano, F. Competition between recovery and Recrystallization. *Materials Science & Engineering A* **333**, 361–367 (2002).
25. Elsey, M., Esedo, S. & Smereka, P. Diffusion Generated Motion for Recrystallization and Grain Growth. *Journal of physics D:Applied physics* 1–24 (2009).
26. Zhang, X., Godfrey, A., Huang, X., Hansen, N. & Liu, Q. Microstructure and strengthening mechanisms in cold-drawn pearlitic steel wire. *Acta Materialia* **59**, 3422–3430 (2011).
27. Li, Y. *et al.* Segregation Stabilizes Nanocrystalline Bulk Steel with Near Theoretical Strength. *Physical Review Letters* **113**, 1–5 (2014).
28. Nematollahi, Gh. A., Grabowski, B., Raabe, D. & Neugebauer, J. Multiscale description of carbon-supersaturated ferrite in severely drawn pearlitic wires. *Acta Materialia* **111**, 321–334 (2016).
29. Hosseini, S. B., Thuvander, M., Klement, U., Sundell, G. & Rytberg, K. Atomic-scale investigation of carbon atom migration in surface induced white layers in high-carbon medium chromium (AISI 52100) bearing steel. *Acta Materialia* **130**, 155–163 (2017).
30. Greer, J. R. & De Hosson, J. T. M. Plasticity in small-sized metallic systems: Intrinsic versus extrinsic size effect. *Progress in Materials Science* **56**, 654–724 (2011).
31. Fritz, R., Maier-Kiener, V., Lutz, D. & Kiener, D. Interplay between sample size and grain size: Single crystalline vs. ultrafine-grained chromium micropillars. *Materials Science and Engineering A* **674**, 626–633 (2016).
32. Yao, H. Y., Yun, G. H. & Fan, W. L. Size effect of the elastic modulus of rectangular nanobeams: Surface elasticity effect. *Chinese Physics B* **22**, 1–5 (2013).
33. Chen, Z. *et al.* Nano-scale characterization of white layer in broached Inconel 718. *Materials Science and Engineering A* **684**, 373–384 (2017).
34. Giallonardo, J. D., Erb, U., Aust, K. T. & Palumbo, G. The influence of grain size and texture on the Young's modulus of nanocrystalline nickel and nickel–iron alloys. *Philosophical Magazine* **91**, 4594–4605 (2011).
35. Barmatz, M. & Chen, H. S. Young's modulus and internal friction in metallic glass alloys from 1.5 to 300 K. *Physical Review B* **9**, 4073–4083 (1974).
36. Armendia, M., Garay, A., Villar, A., Davies, M. A. & Arrazola, P. J. High bandwidth temperature measurement in interrupted cutting of difficult to machine materials. *CIRP Annals - Manufacturing Technology* **59**, 97–100 (2010).

## Figures

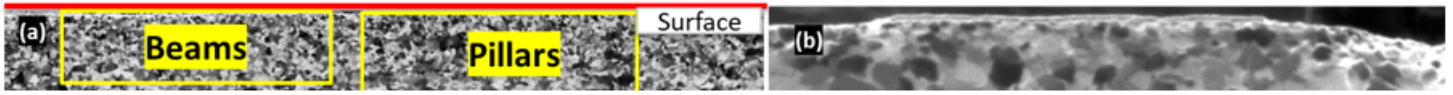


**Figure 1**

Ion image of the chip cross-section machined at 200 m/min. Red dashed line is an estimation of PSZ-SSZ boundary. (b) Detail of the SSZ by ion scanning of chip cross-section when machining at 200 m/min. Crystals tend to equiaxiality and the diameter is consistently in the sub-micrometer regime. Some carbides are present in the structure (red cycles).



**Figure 2**

Images of TEM obtained from the DRX area. STEM image shows the intersection of several grain boundaries and a particle in one of them. EDX chemical maps (center and right side) depict the distribution of iron and carbon atoms. The particle shows a lack of iron and a larger concentration of

carbon, while grain boundaries do not show up in EDX maps indicating the absence of carbon segregation.

### Figure 3

Crystallographic orientation by EBSD on fractioning surface (top correspond to chip-tool contact surface) on chips cut at 200 m/min. (a) Inverse pole figure (IPF) colored in the proximity of the surface and (b) corresponding Kernel average misorientation (KAM) map. (c) IPF and (d) KAM of the whole area affected by friction. (e) and (f) are pole figures (PF) of the area inside and outside of the DRX layer respectively.

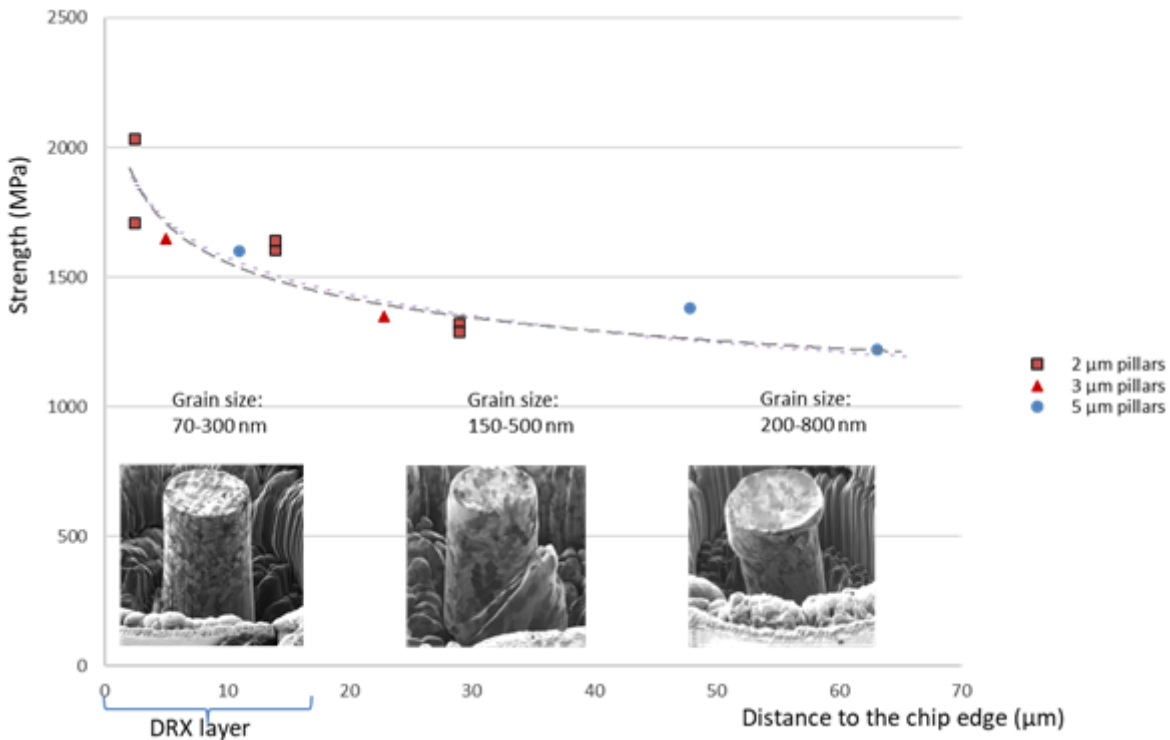


### Figure 4

Strength values obtained by pillar compression tests of the pillars of 2,3 and 6 μm of diameter milled on a cross-section at different depth into the material. Pillar diameter does not have notable influence, however pillar closer to the edge show larger strength.

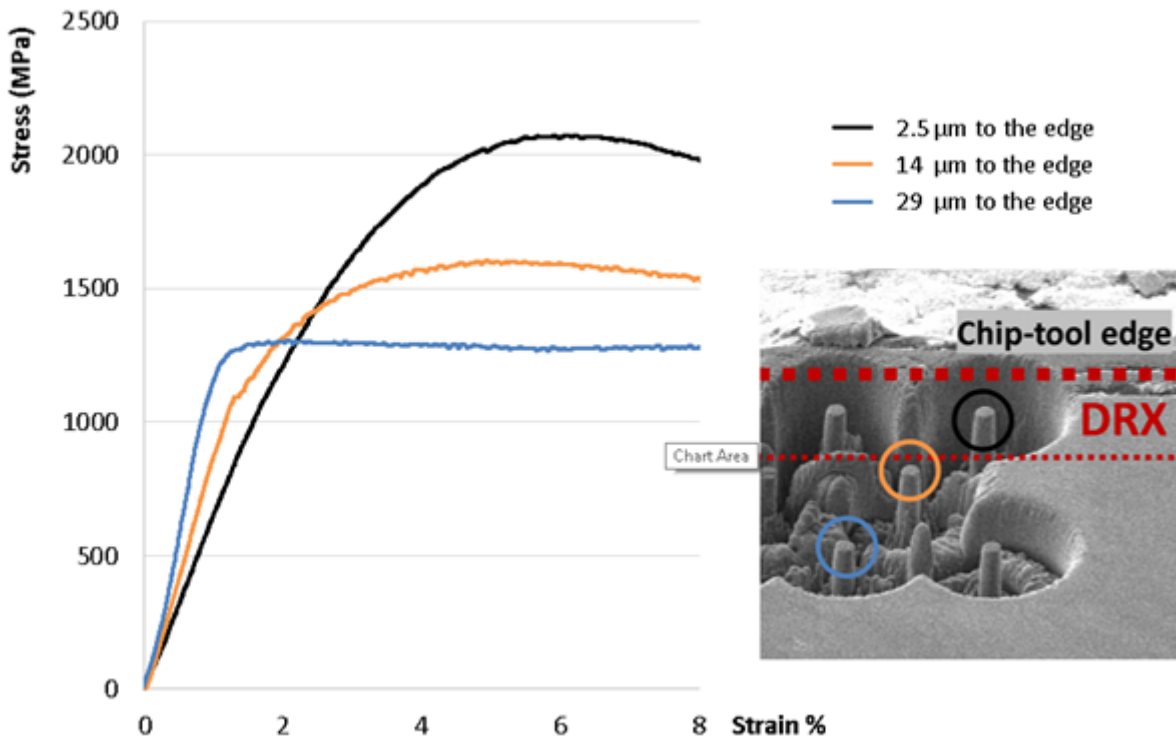


**Figure 5**

The graph shows the stress-strain plot for 2 μm diameter pillars milled at 2.5, 14 and 29 μm from the chip edge.

**Figure 6**

*A pillar (FIB-scanning) image to reveal the grain distribution and the position of pearlite lamellae, locating the area of shear in the interface between ferrite and pearlite. Nanograined steel (a) depicts an homogeneous deformation, while in for larger grains the boundary of pearlite colonies (b) concentrates the shearing (c).*

**Figure 7**

Beam bending experiments for elastic modulus calculation. Left: an SEM image of the bent beam after experiment; right: typical measured strain-stress curve for bending experiment.

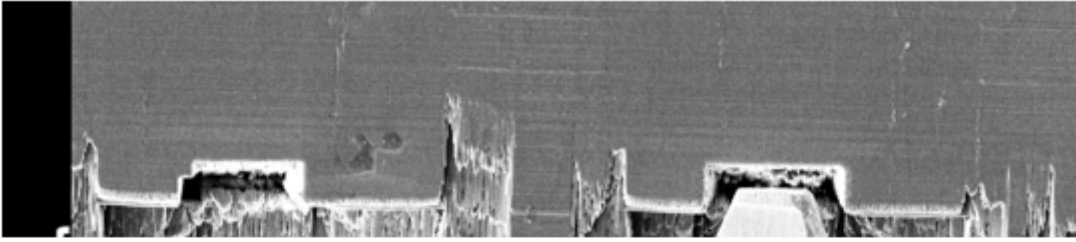


**Figure 8**

Set-up for beam bending in-situ in the SEM experiments . Tip has been fabricated by FIB milling of a tungsten needle.

**Figure 9**

Calculations of the strains for a ASISI 1045 chip cut at 200 m/min and uncut chip thickness of 0.2 mm.